Revision #2 *Word counts (all included) 10551, 11 figures, 2 tables*

Time-resolved Raman and luminescence spectroscopy of synthetic REE-doped hydroxylapatites and natural apatites

Fau A.[(1)], Beyssac O.[(1),*], Gauthier M.[(1)], Panczer G.[(2)], Gasnault O.[(3)], Meslin P.Y.[(3)], Bernard S.[(1)], Maurice S.[(3)], Forni O.[(3)], Boulliard J.C.[(1)], Bosc F.[(4)] and Drouet C.[(4)]

(1) IMPMC, UMR 7590 CNRS - Sorbonne Université - MNHN, Campus Jussieu, Case Courrier 115, 4 place Jussieu, F-75005 Paris (2) ILM, UMR5306 - UCBL – CNRS, 10 rue Ada Byron, F-69622 Villeurbanne (3) IRAP, UMR 5277 CNRS - Université Paul Sabatier Toulouse - CNES, 9 Avenue du Colonel Roche, F-31400 Toulouse (4) CIRIMAT, UMR 5085 CNRS - Université Paul Sabatier Toulouse - INP Toulouse, 4 allée Emile Monso F-31030 Toulouse

** Corresponding author : Olivier.Beyssac@upmc.fr*

Abstract

Using continuous and time-resolved spectroscopy, we investigate Raman and luminescence signals from synthetic hydroxylapatites doped with trivalent REE including Dy^{3+}, Eu^{3+}, Nd^{3+}, and Sm^{3+}, as well as REE in natural apatites, with laser excitations at 532 nm and 785 nm. We demonstrate that time-resolved spectroscopy is an extremely efficient method to tone down the luminescence from Raman spectra or, alternatively, to investigate the luminescence signal without the interference from the Raman contribution. Time-resolved luminescence spectroscopy is found to be a powerful technique for generating specific high-quality luminescence spectra for the REE emission activators in apatites by using appropriate combinations of delay and gate width for the time synchronization of the laser pulse and ICCD detector. This allows for the unambiguous detection and identification of the activators by avoiding the overlapping of various emission signals in the luminescence spectra. This is particularly useful in the case of natural samples, which often have several activators for luminescence. In the case of synthetic REE-doped apatites, a quenching process for luminescence due to activator concentration is seen for Eu^{3+} and Sm^{3+}, i.e. the higher the concentration, the shorter the luminescence decay time. The interpretation of luminescence decay time in natural apatites is promising but more complex because of energy transfers between the various luminescence activators present in the crystal lattice. Luminescence is a powerful technique for detecting the presence of REE in apatites down to ppm levels, though quantifying the concentration is still a challenge.

Keywords: apatite, time-resolved spectroscopy, Raman, luminescence, REE

This is the peer-reviewed, final accepted version for American Mineralogist, published by the Mineralogical Society of America.
The published version is subject to change. Cite as Authors (Year) Title. American Mineralogist, in press.
DOI: https://doi.org/10.2138/am-2022-8006. http://www.minsocam.org/

Introduction

Apatites [$Ca_5(PO_4)_3(F,Cl,OH)$] is one of the most common accessory minerals in both terrestrial rocks and meteorites. They have recently been identified *in situ* on Mars by the ChemCam LIBS instrument onboard the Curiosity rover (Forni et al. 2020). They are also a very important component of bones or teeth as well as a primary source of phosphorous for biological processes. Apatites are sensitive tracers of volatiles and fluid-rock interactions in metamorphic rocks (Harlov 2015), in magmatic and volcanic rocks (Webster & Piccoli 2015) as well as in meteorites (McCubbin & Jones 2015). They are important minerals for thermochronological and geochronological investigations of processes occuring at various depths and temperatures (Chew & Spikings 2015). Last, but not least, apatite offers an unusual range of applications in ecology, agronomy, biology, medicine, archeology, environmental remediation, and materials science (Rakovan & Pasteris 2015; Gomez-Morales et al. 2013). Therefore, it is important to constantly improve the tools used for the characterization of the structure and chemistry of apatites. To this aim, vibrational spectroscopies like infrared and Raman, as well as luminescence spectroscopy, can provide rich amounts of information. This fact, along with a number of practical advantages, nowadays make them useful tools when exploring the physico-chemical properties of apatite.

Raman spectroscopy is useful for a quick, non-destructive and non-ambiguous identification of apatites down to the microscale (Antonakos et al. 2007). In addition, Raman spectroscopy provides valuable information on the presence of OH^- in the halogen site and, more generally, on the type of apatite: hydroxyl- versus fluor- versus chlor-apatite (Antonakos et al. 2007). It can also be used to assess the crystallinity of apatite and to track possible carbonate incorporation in apatite through CO_3^{2-} substitution for PO_4^{3-} tetrahedra (Awonusi et al. 2007, and see Pasteris & Beyssac 2020 and references therein).

Laser excitation during Raman analysis may also induce emission of luminescence in apatite. Luminescence is used here as a generic term describing all kinds of photoluminescence, e.g., fluorescence, luminescence, or phosphorescence (see Gaft et al. 2015 and Waychunas 2014 for further details). Because the luminescence signal can be extremely strong, such that it can completely overwhelm the Raman signal, it is often considered as severely limiting for proper Raman analysis. In some cases, the luminescence peaks can be so sharp that they actually may be confused with Raman peaks (Lenz et al. 2015). However, in many cases luminescence carries rich and valuable information complementary to the data acquired using Raman (Gaft et al. 2015; Nasdala et al. 2004; Panczer et al. 2012; Waychunas 2014). This is particularly the case in apatites (Waychunas

2002; Gaft & Panczer 2013). Recent developments in Raman hyperspectral mapping further allow for the mapping of luminescence patterns in minerals on the microscale, which opens new avenues for the non-destructive investigation of the internal microtexture of minerals (Nasdala et al. 2012; Lenz and Nasdala 2015).

One possible means of avoiding or limiting luminescence is to change the wavelength of the laser excitation used for Raman analysis in the range from the deep ultra-violet (UV) to the near infrared (IR). This approach works well in some cases but it is also limited by severe analytical challenges (e.g. deep UV) or by the poor Raman efficiency at high wavelength in the near IR region (Dubessy 2012; Beyssac 2020 for a review). Another possibility is to use time-resolved (TR) spectroscopy, which utilizes the different lifetimes of the Raman and luminescence processes. The Raman effect is actually a prompt phenomenon with an extremely short lifetime ($\approx 10^{-15}$ s). In contrast, the lifetime of luminescence processes in minerals is longer, ranging from fractions of nanoseconds to seconds and even more (Panczer et al. 2012; Gaft et al. 2015). By perfectly synchronizing in the time-domain a pulsed-laser (in the nanosecond range) with a gated intensified CCD (ICCD), it is possible to excite effectively the Raman effect and to reject efficiently most of the luminescence especially if it has a long decay time. Furthermore, time-resolved spectroscopy makes possible the exploration of the time decay or lifetime of luminescence, which is a measure of the transition probability between two specific levels. Such a lifetime is then a specific and unique property of the luminescence signal (Gaft and Panczer 2013) for a given electronic transition in a precise crystallographic environnement.

Rare-Earth Elements (REE) are a large and very important group of elements in mineralogy and geochemistry. REE incorporation in minerals and exchanges of REE between minerals, melts, and fluids are fundamental in geochemistry and can provide key information on many geological processes. Since they behave as emission centers in minerals, here called luminescence activators, the luminescence properties of REE can be used to detect possible internal zoning in minerals using cathodoluminescence (Waychunas 2014; Gaft et al. 2015) or photoluminescence (Lenz and Nasdala 2015). Because the apatite structure can accommodate a large variety of elements (Hughes and Rakovan, 2015), it is a well adapted matrix for incorporating the REE via two principal coupled substitutions: REE + Na = 2Ca and REE + Si = Ca + P. In fossilized bones for example, REE are progressively incorporated in bone apatite during diagenesis, due to exchange with the surrounding minerals (Suarez et al., 2010). In the field of nanomedicine, the intentional incorporation of luminescent REE as dopants in synthetic bioapatites/bone allows for nanoparticle tracking as a form of medical

diagnosis (Mondéjar et al., 2007, Al-Kattan et al., 2014). The luminescence signal of REE in apatite has recently been exploited, coupled to Raman and histology analysis, to follow the skin penetration of apatite-based colloidal nanoparticles for dermatological applications (Choimet et al. 2020).

Simple yet valuable investigations of luminescence properties in minerals can be done using a conventionnal Raman spectrometer, an instrument largely accessible nowadays in laboratories, and even for field studies (Jehlicka et al. 2017). Notably, there are currently more and more combined Laser-Induced Breakdown Spectroscopy (LIBS) and Raman investigations often combined in a single instrument (see Fau et al. 2019 and references therein). LIBS provides the chemistry and Raman determines the mineralogy. LIBS can detect major and many trace elements but is not able to detect REE at low concentrations. Luminescence spectroscopy can fill the gap and provide detection of REE for such studies. This is particularly the case for the SuperCam instrument, which is an instrumental suite currently deployed on Mars onboard the NASA Perseverance rover. SuperCam combines remote LIBS and time-resolved Raman and luminescence spectroscopy (Wiens et al. 2021, Maurice et al. 2021, Beyssac 2020).

The purpose of the present study is to investigate (i) the structural properties by Raman spectroscopy and (ii) the luminescence properties, of REE in both synthetic REE-doped hydroxylapatites (used as standards) as well as natural apatites. In the case of the synthetic hydroxylapatites, they are doped with trace amounts of one REE, either Eu^{3+}, Sm^{3+}, Nd^{3+} or Dy^{3+}. We also document the decay time of the luminescence signal vs. the concentration of the specific REE. The case of natural apatites is more complex to interpret since several emission centers for luminescence are present within a given sample. Comparison of the time-resolved luminescence spectra between synthetic and natural apatites is first discussed in order to interpret the peaks in the luminescence emission spectra. In addition, we discuss possible factors affecting that the luminescence signal of REE in apatite, in particular those, which control the evolution of luminescence in the time domain like quenching and/or sensitizing phenomena.

An overview on Raman and luminescence in apatite

Apart from a few exceptions, such as end member chlorapatite (monoclinic system, space group $P2_1/b$), apatites generally crystallize with a hexagonal structure in the $P6_3/m$ space group symmetry. The structure contains five crystallographic sites: the Ca1 (9-fold

coordination) and Ca2 (7-fold coordination) sites, the P site, the halogen/OH^- site, and "defect" sites following the terminology by Waychunas (2002). More details on the topology of these sites and, more generally, on the crystal structure of apatites may be found in Hughes and Rakovan (2002, 2015).

The apatite Raman spectrum has been extensively described by O'Shea et al. (1974) and Antonakos et al. (2007). The PO_4^{3-} and OH^- ions in apatite can be easily detected by Raman (Rey et al. 2014). The most intense Raman peak, often used for a quick detection of apatite, is located at ≈ 960 cm^{-1} and is due to the ν_1 symmetric stretching mode of PO_4^{3-}. Additional peaks due to PO_4^{3-} are the doubly degenerate ν_2 bending mode at ≈ 430 cm^{-1}, the triply degenerate antisymmetric ν_3 stretching mode at ≈ 1060 cm^{-1}, and the triply degenerate ν_4 bending mode at ≈ 580 cm^{-1}. OH^-, when present, contributes a large band at ≈ 3570 cm^{-1}, while F^- and Cl^- can not be directly detected by Raman. However, the presence of F^- and/or Cl^- in the OH^- site may induce a shift of the various PO_4^{3-} vibration modes as well as modifications in the OH^- domain due to a modified configuration of hydrogen bonds.

Luminescence of apatites has been extensively studied for a long time (Blasse 1975). Waychunas (2002) and Gaft et al. (2015) made comprehensive reviews while other studies were dedicated to the specific luminescence resulting from Eu (Kottaisamy et al. 1994; Gaft et al. 1997), or more generally to the REE luminescence patterns overall (Reisfeld et al. 1996; Czaja et al. 2010). Other studies have been dedicated to other emission centers in apatite such as U^{6+} and $(UO_2)^{2+}$ (Panczer et al. 1998) or Mn^{2+} (Gaft et al. 2015). Waychunas (2002) provided a detailed description of the luminescence activator types and described their link with the apatite structure. Each of the five sites in apatite can be occupied by activators, but the most common ones, *i.e.* those observed in natural apatites, in particular REE or Mn^{2+}, go in the Ca1 and Ca2 sites (Waychunas 2002).

Luminescence activators for which the change in configurational coordinate between the ground and excited state is small, or even null, will generate very narrow emission lines. This is the case for REE^{3+}, for which (i) the parity forbidden *4f-4f* transitions should be weak unless being enhanced by symmetry crystal fields establishing a relationship between intensity and site symmetry, and (ii) the allowed *4f-5d* transitions generally lead to slightly broader bands. Alternatively, owing to their different localisation within the electronic structure and difference in symmetries between the ground and excited states, some transitions will yield emission bands with much larger widths such as the *d-d* transitions in Mn^{2+}. Activators generally do not behave independently in the apatite structure and some may

transfer part or all of their energy to other nearby activators becoming sensitizers. This applies to some REE^{3+} that can be sensitized by Mn^{2+}. This triggers and enhances emission by REE^{3+} and decreases that of Mn^{2+} (Marfunin 1979). Conversely, some authors have argued that Eu^{2+} can act as a sensitizer of Mn^{2+} luminescence (Knutson et al. 1985; Kottaisamy et al. 1994). Of course, not only a single but a series of REE are generally present in natural apatites making very likely the occurrence of transitions with similar energy. This may favor not only single energy transfer but also multiple ones involving several REE (Waychunas 2002).

In natural apatites, REE can easily substitute for Ca via two coupled substitutions (REE + Na = 2Ca and REE + Si = Ca + P) and become emission centers for luminescence in the crystallographic structure of the host apatite. REE are incorporated in either the Ca1 and/or Ca2 sites and can be luminescent as trivalent or divalent ions. When trivalent REE ions are incorporated in substitution of Ca along with Na or Si (Hosseini et al., 2014), this may generate "abnormalities" or defects in the apatitic lattice altering the local site symmetry (which could have an impact on the luminescence). Studies using steady-state luminescence, *i.e.* continuous excitation in the time domain, generally via UV excitation, have demonstrated that natural apatite luminescence is dominated by divalent Mn^{2+} and Eu^{2+} and trivalent Ce^{3+}, Dy^{3+}, Nd^{3+}, and Sm^{3+} (Gaft et al. 2001). The particular case of Eu substitution in apatite has been extensively studied by Gaft et al. (1997, 2001) and Kottaisamy et al. (1994). These studies give an overview regarding the complexity of REE luminescence in apatite but also provide a great deal of information with respect to this technique. In apatite, Eu^{2+} luminescence appears as a single band at ≈ 450 nm due to a 4*f*-5*d* transition with a lifetime of 500 ns (Gaft et al. 2001). It has been assigned to the Ca2 site by Kottaisamy et al. (1994). Eu^{3+} luminescence is characterized by lines at 590, 617, 651 and 695 nm and was assigned to the Ca1 site (Gaft et al. 2001). In synthetic Eu-doped apatites under a specific excitation, additional lines were observed at 575, 628 and 712 nm and were assigned to Eu^{3+} in the Ca2 site (Morozov et al. 1970).

Synthetic and natural apatite samples

REE-doped synthetic hydroxylapatites

REE-doped hydroxylapatites were synthesized at CIRIMAT Toulouse at relevant geological concentrations, following the method described by Hosseini et al. (2014). The REE selected for this study are trivalent Eu^{3+}, Sm^{3+}, Nd^{3+}, and Dy^{3+} because they are important geochemical tracers and their luminescence patterns in apatite is known. We selected trivalent REE because they emit luminescence in spectral windows relevant to our instrumental setup and

they are also observed in natural samples. The high-purity REE salts used were purchased from SIGMA-ALDRICH. First, we prepared a stock solution of each REE doping element with a concentration of 0.04 mol/L by dissolving respectively europium(III) chloride hexahydrate, ($EuCl_3.6H_2O$ – molecular weight MW: 366.41 g/mol), samarium(III) nitrate hexahydrate, ($Sm(NO_3)_3$ $6H_2O$ - MW: 444.47 g/mol), dysprosium(III) chloride hexahydrate, ($DyCl_3.6H_2O$ - MW: 376.95 g/mol) and neodymium(III) nitrate hexahydrate, ($Nd(NO_3)_3.6H_2O$ - MW: 438.35 g/mol) in deionized water. Preparation of hydroxylapatites was based on coprecipitation obtained by mixing two starting solutions. Solution A contained calcium nitrate tetrahydrate ($Ca(NO_3)_2$.4H2O - MW: 236.15 g/mol) dissolved in deionized water to obtain a Ca concentration of 0.4 mol/L. Solution B contained di-ammonium hydrogenphosphate ($(NH_4)_2.HPO_4$ - MW: 132.06 g/mol) dissolved in deionized water at a phosphate concentration of 0.13 mol/L. REE-doped hydroxylapatites at desired concentrations of the doping element were obtained by mixing solutions A and B and the relevant REE stock solution diluted as necessary and to which 2 mL of 30% NH_4OH ammonia were added to increase the pH of the solution in order to facilitate the hydroxylapatite precipitation. The obtained mixtures are then placed in an oven at 143 °C for a duration of 14 hours. Three successive washing stages with deionized water and centrifugation for 3 minutes at 7500 rpm were carried out in order to remove traces of ammonia and unreacted salts present in the precipitating medium. Finally, the samples were dried in an oven at 80 °C for a minimum of 8 hours.

Natural apatites

The natural apatites (mm to cm in size) were selected from the collection de Minéraux (Sorbonne Université, Paris). Table 1 summarizes the main information for each apatite specimen used. These samples are either single crystals or polycrystalline aggregates.

Methodology

Chemical analyses

Major and trace element analyses for natural and synthetic apatites were done by alkali fusion of rock samples ($LiBO_2$), followed by concentration measurements using an ICP-OES Icap 6500 (Thermoscientific) for major elements, and an ICP-MS X7 (Thermoscientific) for trace elements (protocol by Carignan et al., 2001). Analyses were performed at the Service d'Analyse des Roches et Minéraux (SARM, CNRS, Nancy, France). For the Dy^{3+}-doped synthetic apatite, chemical analysis was performed on only one sample as a luminescence

signal was not detected for these samples (see below). Table 1 and Table 2 present the major (oxide wt%) and trace element (mg/g) composition of the natural and synthetic REE doped samples, respectively. Figure 1 depicts the chondrite normalized REE patterns for the natural apatites.

X-ray diffraction

XRD was used to confirm the crystallography of the synthetic apatites prepared. We used a Panalytical Pro MPD operating at 40 kV, 40 mA with Co-Kα radiation wavelength of λ = 1.788965 Å. Diffractograms were recorded from 5 to 90° in a 2θ scale and 0.033° step size during 3 cycles of 1.5 hour.

Infrared spectroscopy

Fourier transform infrared (FTIR) was used to characterize and verify the crystallinity and molecular structure of the synthetic apatites. We used a Nicolet Magna 560 working under dry air. All measurements were done in transmission mode with a Globar / Nernst lamp source and a DTGS-CsI detector. Spectra were obtained in the 4000-400 cm^{-1} range with a resolution of 2 cm^{-1} and by averaging 200 spectra. Before analyses, samples were prepared by mixing 1 mg of REE-doped hydroxylapatite with 300 mg of dried KBr which was then pressed into pellets and dried at 120°C.

Continuous-wave Raman spectroscopy

All samples were analyzed using a continuous-wave Raman microspectrometer Renishaw InVia Reflex for point analyses and Raman hyperspectral mapping when needed. Measurements were performed using a green 532 nm solid-state laser focused on the sample through a Leica DM2500 microscope with a long-working distance 50X objective (NA = 0.55). This configuration yields a planar resolution of approximately 1-2 µm for a laser power delivered at the sample surface of less than 1 mW using neutral density filters to prevent irreversible thermal damage. This corresponds to a laser irradiance in the range of 0.3 to 1.3 10^9 Wm^{-2}. All measurements were performed with a circularly polarized laser using a ¼-wave plate placed before the microscope in order to minimize polarization effects. The Raman signal was dispersed by a grating with 2400 lines/mm and the signal was analyzed with a RENCAM CCD detector. The spectral resolution for visible light was 1 to 1.9 cm^{-1} and the wavenumber accuracy was better than 0.5 cm^{-1}. Some samples (Nd^{3+}-doped hydroxylapatites)

were also analyzed using a 785 nm diode laser yielding a spot size of a few μm^2 for excitation and a 1200 lines/mm grating for dispersion. The rest of the setup was the same.

For Raman mapping and the acquisition of hyperspectral maps, the sample was moved with an appropriate step size using a XYZ Renishaw motorized stage. Laser focus was optimized by correcting topographic variation prior to analysis (surface mode using the Renishaw Wire 4.3 software) and all maps were processed using the Wire 4.3 software. More details concerning the Raman mapping technique can be found in Bernard et al. (2008). All measurements were performed at room temperature and spectra were recorded directly on the raw samples without any preparation. Note that continuous-wave Raman spectroscopy also provides steady-state luminescence emission spectra in the range 532-720 nm with excitation at 532 nm, or in the range 785-930 nm with excitation at 785 nm.

Time-resolved Raman and luminescence spectroscopy

All samples were also analyzed using a custom-built, time-resolved Raman and luminescence spectrometer as described by Fau et al. (2019). The laser is a nanosecond (1.2 ns FWHM, 1 mJ per pulse) pulsed, diode-pumped, solid-state (DPSS) laser operating at 532 nm with a 10 to 2000 Hz repetition rate. The laser is slightly defocused at the sample surface through a microscope objective (MPlan Apo Mitutoyo 20X, NA= 0.42). The Raman and luminescence signals are collected using a backscattering geometry. In addition, the laser was circularly polarized thanks to a ¼-wave plate placed before the microscope in order to minimize polarization effects. In this setup, a Notch filter cut off the Rayleigh scattering at ≈ 90 cm^{-1}. The signal was collected using an optical fiber and sent into a modified Czerny-Turner spectrometer (Princeton Instruments IsoPlane 320) coupled with an intensified Princeton Instruments PIMAX4 ICCD camera. The fine control of both the time delay and the gating time of the camera allows for sub-nanosecond time resolution experiments thanks to a precise synchronization between the laser pulse and the ICCD. This spectrometer has three motorized gratings, which can be selected depending on the spectral window and resolution required for the measurement. In this study, we mostly used a 600 lines/mm grating yielding a spectral resolution of 10-13 cm^{-1}. Irradiance, associated with a pulsed laser, can be estimated as $Q/(\tau S)$, with $Q = P/f$ being the laser energy per pulse, P being the time-integrated laser power measured at the surface of the sample, f the laser repetition rate, τ the pulse duration, and S the surface area of the laser spot on the sample. For these experiments, irradiance was set at ≈ 10^{10} Wm^{-2}, which is a conservative value even in the case of absorbing minerals (Fau et al. 2019).

306

307 ## Time-resolved Raman and luminescence spectroscopy: overview

308 The luminescence signal is generally much stronger than the extremely weak Raman signal.
309 One way to separate the Raman signal from the luminescence signal is to exploit the fact that
310 these two processes have very different lifetimes using time-resolved spectroscopy. Lifetime
311 corresponds to the time spent in any excited state, *i.e.* vibrationnal for Raman and electronic
312 for luminescence, before it returns to the ground state. For luminescent compounds, de-
313 excitation is expected to occur by the emission of a photon. However, depending on the
314 energy gap between the excited and ground states of a given luminescent center (e.g. Eu^{3+} or
315 Tb^{3+} ions), de-excitation may partially also occur by a non-radiative process such as in the
316 form of vibrational energy (phonon) if a good energetic correspondence is found. This has
317 been reported in apatites with O-H vibrations (Al-Kattan et al., 2014). However, even in this
318 case, luminescent signals remain strong. In all cases, light absorption is "immediate" in the
319 range of 10^{-18} seconds, while Raman and the emission of luminescence are longer processes.
320 Relaxation from virtual vibrational levels is typically in the range of 10^{-15} seconds for Raman
321 and can be considered as "immediate" on our experimental time scale. On the other hand,
322 going back from excited electronic levels to the ground state is a much slower process, such
323 that the lifetime of luminescence can cover a wide time range from the nanosecond (e.g.,
324 organic fluorescence, Lakowicz 2006) to milliseconds or even seconds (e.g., Cr^{3+} or REE^{3+} in
325 minerals, Gaft et al. 2015).

326 Time-resolved spectroscopy uses a pulsed excitation signal synchronized with a gated
327 detector. The main idea is that the Raman signal will last only during the excitation pulse,
328 while the luminescence will be excited within the pulse but will continue to emit and decay
329 after the pulse. Using a short time gate perfectly synchronized with the laser pulse and
330 matching it in the time domain allows for rejection of most of the luminescence signal and the
331 maximization of the collection of the Raman signal. Time-resolved spectroscopy further
332 allows for the collection of only the luminescence signal, without any Raman contribution, by
333 simply opening the detector gate just after the laser pulse. The Raman signal has then
334 completely vanished and is absent in the spectrum while the luminescence is still present.

335 In this study, we investigate the emission spectra, which were obtained with an incident
336 excitation laser at 532 nm, or 785 nm in the case of Nd^{3+} using the continuous-wave
337 spectrometer. Such excitation wavelengths are likely not optimal for triggering absorption and
338 thereby emission of luminescence. Using UV would be more efficient, but these wavelengths
339 constitute a good compromise for combining Raman and luminescence investigations. The

custom-built time-resolved instrument used for this study offers an excellent synchronization making possible the exploration of luminescence with various lifetimes. To this aim, an appropriate combination of delays (the moment the detector gate opens with respect to the laser pulse) and the gate width has to be used.

Lastly, this technique allows for the proper characterization of the decay time of the luminescence by doing time sweep experiments. A post-pulse detector gate with an appropriate opening duration is shifted for various time delays, and the integrated intensity of the signal can be plotted versus the shift time (delay). These data allow for the lifetime to be calculated and give further information on the nature of the electronic transition and, more practically, on the identification of the emission center (Lakowicz 2006; Gaft & Panczer 2013; Gaft et al. 2015).

Luminescence decay is given by

$$I(t) = I_0 e^{-\frac{t-t_0}{\tau}} \quad (1)$$

with I_0 being the number of photons emitted at time t_0, and τ the lifetime of the considered transition. Analysis of the luminescence decay is done by measuring the number of photons received during a period of time controled by the gate width and by shifting this gate through time after the laser pulse. Critical parameters are then the gate width t_g and the time increment t_s by which the gate is shifted.

Using the time-resolved setup one effectively measures:

$$F(T) = \int_T^{T+t_g} I_0 e^{-\frac{t-t_0}{\tau}} dt \quad (2)$$

in n+1 points given by

$$T_k = t_0 + k\, t_s \quad (3)$$

After normalisation by the gate width and the introduction of equation (3), F(T) becomes

$$F(T_k) = I_0 t_g e^{-\frac{kt_s}{\tau}} \left(\frac{1-e^{-\frac{t_g}{\tau}}}{\frac{t_g}{\tau}} \right) \quad (4)$$

Several aspects about the methodological information can be retrieved from this equation. First, the gate width does not influence the experimental evaluation of τ because whatever the value of τ, $\left(\frac{1-e^{-\frac{t_g}{\tau}}}{\frac{t_g}{\tau}} \right)$ is a constant value even if $\frac{t_g}{\tau}$ is large. For a reliable assesment of τ, luminescence must have decayed notably so that $\frac{kt_s}{\tau} > \frac{1}{4}$. To have an acceptable uncertainty, the statistics have to be good, and so the k value has to be large. Lastly, the unpredictable factor is the intensity of the luminescence. The lower the intensity, the larger the signal

accumulation time required to obtain a correct spectrum. This is an important parameter to consider in such experiments, which has an important effect on the duration of the decay time experimental analysis (time sweep experiment).

To exploit efficiently the luminescence spectra and the time sweep experiments, a specific script was written using Python. A Voigt function is used for fitting all peaks and includes a Gaussian component with a fixed FWHM value at 13 cm^{-1} corresponding to the instrument resolution and a Lorentzian component due to the luminescence signal. A linear baseline defined by two points, automatically calculated as the lowest points from a predefined region in the spectrum, was subtracted prior to the luminescence peak fitting. No normalization was performed before data processing. For each time sweep experiment, the selected peaks were fitted on the first spectrum of each series, when the signal-to-noise ratio is high, by leaving free the Lorentzian FWHM as well as the area and position of the Voigt band. A second series fit is then performed on the whole series of spectra with just the Voigt band area as a free parameter. Lifetime is determined from the semi-logarithmic representation of the intensity versus time delay and is taken as the slope of the regression line extracted from the experimental points.

In addition, time-resolved spectroscopy allows for the exciting selection of luminescence emissions from various emission centers if they have different decay lifetimes. This is a very promising approach for the interpretation of luminescence spectra, especially in the case of apatites, since emission peaks from various emission centers often overlap in the spectral domain.

Results

Physico-chemical characterisation of the REE-doped synthetic apatites

XRD diffractograms of synthetic hydroxylapatites display all the main characteristic peaks of hydroxylapatite thus confirming their crystallinity (Figure 2). These finding are corroborated by FTIR spectroscopic analyses (Figure 3). All the infrared spectra obtained are very similar for the different synthetic hydroxylapatites and exhibit the spectral features characteristic of hydroxylapatite (Rey et al., 2014). This is seen in the presence of an OH^- peak at 3570 cm^{-1} (O-H stretching) and an associated libration band at 632 cm^{-1}. The presence of trace impurities in the form of nitrate NO_3^- ions is detectable as a minor contribution (≈1383 cm^{-1}). In addition, the presence of H_2O in the synthetic apatites is detectable via a wide band due to the vibration of H_2O molecules at around 3400 cm^{-1}.

Chemical data obtained for the major and trace elements in the synthetic hydroxylapatites are presented in Table 1. Table 1 shows that the range of concentrations obtained for Eu^{3+}, Sm^{3+}, Dy^{3+}, and Nd^{3+} varies from tens to thousands of ppm. However, the luminescence signal for Dy^{3+} was not detected (see below). We also note that some hydroxylapatites were slightly contaminated by another REE than the one used for the synthesis. This is likely due to impurities in the REE salts used in the synthesis. For instance, the sample of hydroxylapatite doped with a concentration of 24 ppm of Sm also has a Eu concentration of around 5 ppm. Continuous-wave Raman mapping was performed on some of the synthetic hydroxylapatites in order to assess their homogenity by obtaining thousands of spectra from a given sample. These maps showed that the chemical composition of these samples is homogeneous because the FWHM and peak position of the main ν_1 peak is constant with only minor variations (<1 cm^{-1}).

Time-resolution Raman spectroscopy

Figure 4 depicts representative continuous-wave micro-Raman spectra obtained at random positions on the synthetic hydroxylapatites. The Raman signal remains constant in the Raman shift for all the synthetic hydroxylapatites, while the luminescence emission after light absorption strongly depends on the excitation wavelength for each REE. Eu^{3+} ions are highly excited at 532 nm and luminescence completely masks the Raman signal (Figure 4a) while for Sm^{3+} luminescence is less strong and the Raman signal is visible (Figure 4b). In the case of Dy^{3+}-doped apatites, 532 nm is out of the range of absorption (excitation) and emission of luminescence is not observed while the Raman bands are plainly visible (Figure 4c). Note that the case of Nd^{3+} is different. Raman peaks are clearly visible when excited at 532 nm but non-visible with excitation at 785 nm because the luminescence of Nd^{3+} is extremely strong in the near IR region (Figure 4d).

Figure 5 shows a representative Raman spectrum obtained with the time-resolved Raman instrument with a short gate (5 ns) centered on the laser pulse. This spectrum was obtained with a highly luminescent hydoxylapatite doped with 23,936 ppm Sm^{3+}. Similar spectra were obtained for all the other synthetic doped hydroxylapatites. The difference is striking with continuous-wave Raman spectroscopy as no luminescence bands are detected while all the Raman peaks are clearly visible, including the OH^- bands. This is due to the efficient rejection of the longer lasting REE luminescence.

The case for natural apatites is more complex when analyzed with continuous-wave Raman spectroscopy (Figure 6). A very strong background, including some peaks due to

Raman and luminescence, is observed in all the spectra. In general, only the main ν_1 symmetric stretching mode of PO_4^{3-} is observed in all these these spectra while the other stretching modes are hardly detected in some of the samples (Slyudyanka and Imilchil). Clearly, using time-resolved Raman spectroscopy makes possible the rejection of almost all the luminescence contributions in these natural apatites and the recording of high-quality Raman spectra without any luminescence interference. It is particularly interesting in the case of the REE because they generate intense, thin peaks that can be easily confused with Raman peaks in phosphate minerals but also in other mineral phases like zircon as discussed by Lenz et al. (2015).

In the REE-doped synthetic hydroxylapatites, the Raman shift of the ν_1 symmetric stretching mode of PO_4^{3-} is nearly constant at about 960 ± 1 cm^{-1}. In the natural apatites, this PO_4^{3-} mode is in the range 963.8 to 965.4 cm^{-1}. A strong OH^- band is observed in all the synthetic apatites while it is not observed in the natural apatites, nor in the time-resolved Raman spectra. The Raman shift of the ν_1 symmetric stretching mode for PO_4^{3-} is actually sensitive to the nature of the apatite (Ashley et al. 2018). It occurs at ≈ 960 cm^{-1} in pure hydroxylapatite, ≈ 961 cm^{-1} in pure chlorapatite, and ≈ 965 cm^{-1} in pure fluorapatite. This is due to the fact that Cl^- has a much larger ionic radius compared to F^-. From these observations, Raman investigations confirmed that the synthetic apatites are pure hydroxylapatites as assessed from infrared and XRD characterization. The natural apatites are solid solutions in between the three endmembers (OH^--Cl^--F^- apatites), though the Raman spectra do not show a notable contribution of OH^- (Figure 6). Based on the Raman shift of the ν_1 symmetric stretching mode of PO_4^{3-}, most natural samples appear to have Raman shift values corresponding to high levels of F^- in the halogen site and these samples likely correspond essentially to fluorapatites. Only the case of the Imilchil sample is slightly different with a lower shift and this sample has likely a higher Cl^- level in the halogen site.

Discussion

Time-resolved luminescence for detecting REE and other emission centers

If time-resolved spectroscopy allows for luminescence features in Raman spectra to be eliminated, it can also eliminate the Raman contribution from luminescence spectra. In order to accomplish this, the ICCD gate has to be opened after the laser pulse when the Raman signal is is no longer active. For many minerals, including apatite, the main luminescence

emission lines can be assigned rather confidently unless there is a strong overlap between the various luminescence signals, which then makes the interpretation complex (Gaft et al. 2015).

In the natural apatites, the total Raman and luminescence spectra obtained using continuous-wave illumination is actually not staightforward to interpret (Figure 6). This is due to the multiple emission lines of the various REE incorporated in the mineral structure (Figure 1) in addition to the possible contribution from other activators like Mn^{2+}. Mn^{2+} is actually likely partly responsible for the broad background observed in some of the natural apatites. Figure 7 illustrates the capability of time-resolved spectroscopy to separate the Raman signal from the luminescence signal in the Durango apatite. In addition, this technique allows further investigations of the luminescence by generating spectra specific to activators with various lifetimes by selecting appropriate combinations of delays and gates. In the case of the Durango apatite (Figure 7), this technique allows for the retrieval of a clear spectrum from the short-lifetime luminescence signal due to Er^{3+} by opening a short gate (1,500 ns) just after the laser pulse (delay 6 ns). Erbium luminescence is otherwise completely covered by longer lifetime emissions in the continuous wave emission spectrum. In a complementary approach, this technique allows for analysis of long lifetime emissions by opening a wide gate (450,000 ns) long after the laser pulse (delay 1,500 ns). Ideally, if activators are expected in a given sample and the approximative lifetime of their emission is known, appropriate combinations of delay and gate should allow for maximization of the emission signal for each activator. This makes time-resolved spectroscopy an extremely powerful tool for avoiding the overlapping of various luminescence contributions from REE and other emission centers in both apatites and other mineral phases.

Alternatively, at a constant delay (e.g. just after the laser pulse) one can open the gate with increasing values from 10 to thousands of ns (here we limit at 450,000 ns just before the next laser pulse arriving at 500,000 ns at 2 KHz) in order to test the detection of various emission centers with different lifetimes. This is illustrated in Figure 8 for the Durango apatite. With short gates (<1,000 ns), only a short lifetime emission signal, here Er^{3+}, is visible in the spectrum because of the less efficient rejection of short lifetime luminescence. Increasing the gate width allows for the detection of other peaks corresponding to longer lifetime emission signals from Sm^{3+}, Eu^{3+}, and Dy^{3+}. This approach is useful for obtaining neat emission spectra for short lifetime emissions, and also for assessing the rejection efficiency of the instrumental time resolution.

Luminescence spectra retrieved from the synthetic REE-doped hydroxylapatites are easier to interpret (Figure 4). In the case of Eu^{3+}, a strong luminescence signal is observed at

all concentrations including the lowest (Figure 4a). This signal is composed of several bands with two main emission bands centered at 590 and 620 nm corresponding to the $^5D_0$-$^7F_1$ and $^5D_0$-$^7F_2$ transitions, respectively. Other less important peaks are observed at ≈ 655 nm and ≈ 570-580 nm and correspond to $^5D_0$-$^7F_3$ and $^5D_0$-$^7F_0$ transitions, respectively. The case of Sm^{3+} is very similar to that of Eu^{3+} with two main emission bands occurring at ≈ 600 and 650 nm (Figure 4b). Dy^{3+} has no emission bands in any of the spectra even at concentrations as high as 500 ppm (Figure 4c). It contrasts with natural apatites in which Dy^{3+} emission bands were observed at ≈ 590 nm (Figure 8). One possible explanation is that emission by Dy^{3+} is sensitized either by another REE and/or by Mn^{2+} in the natural samples. Marfunin (1979) and Waychunas (2002) have actually reported that Mn^{2+} can act as a sensitizer for the luminescence of some REE: Mn^{2+} absorbs incident energy and transfers it to the REE, which then emit light. In the case of the synthetic hydroxylapatite, Dy^{3+} is the only doped element and therefore is not excited. In the case of Nd^{3+}, the luminescence peaks are detected only with a continuous-wave instrument with an excitation at 785 nm in the near infrared part of the spectrum. This sample could not be studied with the time-resolved instrument (excitation at 532 nm). The Nd^{3+} emission is characterized by an intense, broad emission band with several peaks in the range 850 to 925 nm (Figure 4d).

Fitting luminescence spectra

A simple visual inspection of the spectra shows that (i) luminescence spectroscopy is extremely sensitive down to the ppm level and (ii) the overall intensity of the luminescence signal dramatically increases with the activator concentration. Figure 9 depicts the total intensity (sum of areas for all peaks after peak fitting) of the luminescence signal for the emission bands centered at 620 nm and 600 nm as a function of the Eu^{3+} and Sm^{3+} concentrations, respectively. In Figure 9, the luminescence signal was analyzed using continuous-wave spectroscopy and time-resolved spectroscopy with a laser repetition rate of 100 Hz. While in the former case, the excitation/collection is continuous, in the latter case the signal was mostly generated by a single laser pulse as the signal has almost completely decayed between two pulses. There is a sharp increase in the luminescence intensity with increasing concentration of the specific REE. The higher the concentration, the stronger the luminesce signal is. It is challenging to retrieve any quantitative information from this observation as the absolute intensity of the signal depends on many other parameters such as the state of the sample surface, the grain size, the sample effective optical absorption, or the sample orientation with respect to the incident laser beam.

Using the developed Python script, the Eu^{3+} and Sm^{3+} spectra from the synthetic hydroxylapatites at different concentrations and different delays of the time sweep experiments were deconvoluted. For Eu^{3+}, the fit was performed on the emission band centered at 620 nm with 8 bands while it was done on the emission band centered at 600 nm for Sm^{3+} with 5 bands. This is a rather challenging task as these emission bands are likely generated by a much larger number of electronic transitions. For instance, Sm^{3+} luminescence in apatite results from a large number of f-f electronic transitions. The $4f^5$ configuration of Sm^{3+} ion has at least 73 multiplets yielding 198 energy levels via spin-orbit interactions (Axe and Dieke, 1962). Not all these transitions are excited and not all of them will generate emission if excited. The number of bands selected may appear somewhat arbitrary, however it is determined by what is actually observed in the spectra. First, in both the Eu^{3+} and Sm^{3+} cases, it was observed that within a specific emission band, all the peaks decay with the same lifetime. Second, to investigate the effect of the activator concentration, several plots of the various peaks FWHM or relative intensities were made. In general, no significant trends were observed except for an increase of the 597 nm/604 nm peak area ratio in the case of Sm^{3+}.

One purpose of these investigations was to check for possible correlations between any spectral parameter and the luminescence activator concentration. This would provide a proxy for quantification or semi-quantification of the activator thanks to its luminescence signal. No such correlation was found for the spectral parameters. This contrasts with the Cr^{3+} luminescence in Al_2O_3 quenched glasses doped at various concentrations of Cr^{3+}. Cr^{3+} luminescence in ruby has been extensively studied and results from optical absorption into the $^4T_2$ and $^2T_2$ levels and the two well-known emission bands R1 (at 694.25 nm at 300 K) and R2 (at 692.74 nm at 300 K) originate from the ^2E level (see Syassen 2008 and references therein). Chervin et al (2001) studied the spectral parameters of emission spectra of Al_2O_3 quenched glasses prepared as micro-spheres doped with various concentrations of Cr^{3+} as a pressure gauge for optically transparent high-pressure diamond anvil cells. They established clear correlations between the Cr^{3+} concentration and the FWHM of both the R1 and R2 emission lines at various excitation energies. The higher the concentration was, the broader the two lines were. Such correlations can be used as a first-order proxy for Cr^{3+} concentration in ruby glasses.

In the case of natural apatites, the situation is even more challenging due to the multiple overlapping luminescence signals detected in these samples. If time-resolved spectroscopy can be used to discriminate between short versus long lifetime signals in the emission spectra, one challenge is that many overlapping REE emission signals have similar

This is the peer-reviewed, final accepted version for American Mineralogist, published by the Mineralogical Society of America.
The published version is subject to change. Cite as Authors (Year) Title. American Mineralogist, in press.
DOI: https://doi.org/10.2138/am-2022-8006. http://www.minsocam.org/

lifetimes both amongst themselves and with other emission signals (e.g. Mn^{2+}) making the fitting of any spectra a challenge.

Interpretation of the luminescence lifetime

Time sweep experiments were performed on the natural and synthetic apatites on order to investigate the lifetime of the Eu^{3+} and Sm^{3+} emission. For this, the laser repetition rate was set at 200 Hz. Twenty spectra with a gate of 1 ms were taken with the first being recorded 200 µs after the laser pulse and the delay being augmented by 200 µs for each successive spectrum with a final spectrum at 4 ms after the pulse. The total intensities of the 8 peaks composing the emission band at 620 nm for Eu^{3+} and of the 5 peaks of the emission band at 600 nm for Sm^{3+} are plotted against time (here the delay) as represented in Figure 10. For both Eu^{3+} and Sm^{3+}, the higher the concentration of the activator, the faster the decay of the luminescence. From Figure 10, the luminescence lifetime for each decay curve for Eu^{3+} and Sm^{3+} can be calculated from equation (4) and plotted against the activator concentration as shown in Figure 11. In both cases, there is a clear correlation between the luminescence lifetime and the activator concentration, even at low concentration. The higher the concentration is, the shorter the luminescence lifetime. Such an acceleration of the decay of the luminescence signal by increasing the concentration of the activator may be a consequence of a concentration quenching effect. By increasing the number of activators in the mineral structure, some activators may directly transfer their excitation energy to a neighbour activator through a non-radiative process, *e.g.* by a vibrationnal process. Such a correlation has already been observed for other materials like $Gd_2O_3:Eu^{3+}$ nanocrystals (Meza et al. 2014). These authors established a clear correlation between the lifetime and Eu^{3+} concentration from experimental data that they were able to model using a simple rate equation model. They interpreted such correlation as the consequence of a concentration quenching involving energy transfer among Eu^{3+} ions but also with O^{2-}. Also, as mentioned above, in hydroxylapatites, part of the de-excitation energy may contribute to some O-H stretching, which has been seen in deuterated experiments (Al-Kattan et al., 2014).

Time sweep experiments were run with the natural apatites in the same configuration as the one used for the synthetic samples. The Eu^{3+} emission band at 620 nm and the Sm^{3+} emission band at 600 nm were fitted following the procedure used previously in the case of the synthetic hydroxylapatites. Time decay figures can be generated for each natural apatite (not represented here) and the lifetime of Eu^{3+} and Sm^{3+} emission signals can be calculated. Several spots were analyzed on each natural apatite in order to have an insight into the intra-

sample chemical and structural heterogeneity. Figure 11 depicts all the calculated lifetimes for both the natural apatites and the synthetic hydroxylapatites for Eu^{3+} and Sm^{3+} luminescence versus the concentration in Eu^{3+} and Sm^{3+} measured by ICP-MS (Table 1 and 2). First of all, the natural apatites show a systematic, significant dispersion for the calculated lifetimes compared to synthetic hydroxylapatites. Notably, in the case of Eu^{3+}, the concentrations observed in the natural apatites are lower than those in the synthetic ones (Figure 11a). In addition, for Eu^{3+}, the scattering of the lifetime values for natural apatites covers a range almost similar to the complete range of lifetime values in the synthetic hydroxylapatites. This dispersion may reflect the intra-sample chemical zoning for REE, which is often observed in natural apatites. More generally, there is no clear correlation between the lifetime and the activator concentration for the natural apatites. The points retrieved from the natural apatites do not fall on the correlation observed with the synthetic hydroxylapatites. They are generally above the curve obtained from the synthetic samples, which means that the luminescence generally takes longer to decay in natural apatites compared to the synthetic hydroxylapatites.

A major difference between the natural apatites and synthetic hydroxylapatites is the presence in the former of several REE activators and even sometimes of other activators like Mn^{2+}, while the synthetic hydroxylapatites are doped with a single activator apart from the minor impurities mentioned above. There is no easy interpretation for this difference in luminescence behavior but likely there is a complex interplay between the various activators in the natural samples involving a sensitizing and/or quenching processes for luminescence among the REE and/or with other activators. For instance, using time-resolved spectroscopy, Czaja et al. (2010) demonstrated the effective energy transfer between Pr^{3+} and Sm^{3+} in natural apatites and showed its effect on the lifetime of emission luminescence from these crystals. Such effects are absent in the synthetic hydroxylapatites, which are doped with a single REE activator.

As already mentionned by Gaft and Panczer (2013), it is important to distinguish a theoretical “true” decay time or lifetime from a real effective decay time or lifetime. The true lifetime is an intrinsic physical parameter of a given transition for an activator in a crystal lattice in the absence of any non-radiative processes and obtained under precise conditions (e.g. temperature, pressure). The effective lifetime is the one measured in the laboratory that can be close to the true one in the case of “perfect” samples with one single activator and no other impurities. But it can be very different in the case of natural samples. The effective lifetime is influenced primarily by external parameters like temperature or analytical parameters, such as the orientation of the crystal with respect to the polarization of the

incident laser beam. Also, irradiance may play a role. Overall, as shown by this study, it can depend on the internal properties of the samples like the presence of other impurities (other activators, defects), which may trigger complex sensitizing and/or quenching phenomena via energy transfer.

Implications

Time-resolved spectroscopy is a very powerful tool which combines both Raman and luminescence spectroscopy (Figure 7). Time-resolved spectroscopy is extremely efficient in the detection and identification of REE in accessory mineral such as apatites, other phosphate minerals, titanite, or zircon. Owing to its capability to scan the time domain and selectively analyze each emission signal (Figure 7 and 8), time-resolved spectroscopy provides information that is not accessible to steady-state, *i.e.* continuous-wave, spectroscopy. A major achievement would be to reach some quantification, or at least semi-quantification of luminescence activators in mineral phases from the luminescence signal, either directly from the spectra or through the study of luminescence lifetime. This may be possible in the case of systems involving one single activator such like Cr^{3+} in natural or synthetic ruby, or in our synthetic REE-doped hydroxylapatites. It is a complex challenge in systems involving more than one activator as activators are likely to transfer energy among themselves generating complex quenching and/or sensitizing interactions and thus adding layers of complexity to the interpretation of the time-resolved data.

Currently, the Mars2020 SuperCam time-resolved instrument onboard the NASA Perseverance rover on Mars should benefit from time-resolved Raman and luminescence spectroscopy for detecting and investigating REE in phosphate and other minerals in martian rocks thereby opening new avenues for our understanding of the geochemical processes at work on this planet (Wiens et al. 2021; Maurice et al. 2021).

Acknowledgements

The first author was supported by the Labex Matisse (ANR-11-IDEX-0004-02). Funding of this research by Sorbonne Université and CNRS INP is acknowledged. This paper benefited from comments by Christoph Lenz and an anonymous reviewer as well as from thorough reading by Editor Daniel Harlov.

References

Al-Kattan, A., Santran, V., Dufour, P., Dexpert-Ghys, J., and Drouet, C. (2014) Novel contributions on luminescent apatite-based colloids intended for medical imaging. Journal of Biomaterials Applications, 28, 697-707.

Antonakos, A., Liarokapis, E., and Leventouri, T. (2007) Micro-Raman and FTIR studies of synthetic and natural apatites. Biomaterials, 28, 3043–3054.

Ashley, K.T., McKeeby, B.E., Harlov, D.E., Bodnar, R.J., and Ramsey, M.S. (2018) High-Resolution Raman Spectroscopy Constraints on Apatite Halogen Composition: Implications for Planetary Volcanism and Igneous Processes. Abstract for the Lunar and Planetary Science Conference, Houston, USA, 1483.

Awonusi, A., Morris, M.D., and Tecklenburg, M.M.J. (2007) Carbonate Assignment and Calibration in the Raman Spectrum of Apatite. Calcified Tissue International, 81, 46–52.

Axe, J.D., and Dieke, G.H. (1962) Calculation of Crystal - Field Splittings of Sm^{3+} and Dy^{3+} Levels in LaCl3 with Inclusion of J Mixing. Journal of Chemical Physics, 37, 2364–2371.

Bernard, S., Beyssac, O., and Benzerara, K. (2008) Raman Mapping Using Advanced Line-Scanning Systems: Geological Applications. Applied Spectroscopy, 62, 1180–1188.

Beyssac, O. (2020) New trends in Raman spectroscopy: from high-resolution geochemistry to planetary exploration. Elements, 16, 117-122.

Blasse, G. (1975) Influence of local charge compensation on site occupation and luminescence of apatites. Journal of Solid State Chemistry, 14, 181–184.

Carignan J, Hild P, Mevelle G, Morel J, and Yeghicheyan D (2001) Routine analyses of trace element in geological samples using flow injection and low pressure on-line liquid chromatography coupled to ICP-MS: a study of geochemical reference materials BR, DR-N, UB-N, AN-G and GH. Geostandards Newsletter, 25, 187-198.

Chervin, J.C., Canny, B., and Mancinelli, M. (2001) Ruby-spheres as pressure gauge for optically transparent high pressure cells. High Pressure Research, 21, 305–314.

Choimet, M., Tourrette, A., Marsan, O., Rassu, G., and Drouet, C. (2020) Bio-inspired apatite particles limit skin penetration of drugs for dermatology applications. Acta Biomaterialia, 111, 418-428.

Chew, D.M., and Spikings, R.A. (2015) Geochronology and Thermochronology Using Apatite: Time and Temperature, Lower Crust to Surface. Elements, 11, 189–194.

Czaja, M., Bodył, S., Lisiecki, R., and Mazurak, Z. (2010) Luminescence properties of Pr^{3+} and Sm^{3+} ions in natural apatites. Physics and Chemistry of Minerals, 37, 425–433.

Dubessy, J., Caumon, M-C., Rull, F., and Sharma, S. (2012) Instrumentation in Raman spectroscopy: Elementary theory and practice. In: Dubessy, J., Caumon, M-C., Rull, F. (eds)

719 Raman Spectroscopy Applied to Earth Sciences and Cultural Heritage, p. 83-172, European
720 Mineralogical Union and Mineralogical Society of Great Britain & Ireland, London.
721
722 Fau, A., Beyssac, O., Gauthier, M., Meslin, P.Y., Cousin, A., Benzerara, K., Bernard, S.,
723 Boulliard, J.C., Gasnault, O., Forni, O., Wiens, R.C., Morand, M., Rosier, P., Garino, Y.,
724 Pont, S., and Maurice, S. (2019) Pulsed laser-induced heating of mineral phases: Implications
725 for laser-induced breakdown spectroscopy combined with Raman spectroscopy.
726 Spectrochimica Acta Part B: Atomic Spectroscopy, 160, 105687.
727
728 Forni, O., Meslin, P.-Y., Drouet, C., Cousin, A., David, G., Mangold, N., Dehouck, E.,
729 Rampe, E.B., Gasnault, O., Beck, P., Nachon, M., Newsom, H., Blaney, D. L., Clegg, S. M.,
730 Ollila, A.M., Lasue, J., Maurice, S., and Wiens, R.C. (2020) Apatites in Gale Crater. Abstract
731 for the Lunar and Planetary Sciences Conference, Houston, USA, 2192.
732
733 Gaft, M., and Panczer, G. (2013) Laser-induced time-resolved luminescence spectroscopy of
734 minerals: a powerful tool for studying the nature of emission centres. Mineralogy and
735 Petrology, 107, 363–372.
736
737 Gaft, M., Panczer, G., Reisfeld, R., and Uspensky, E. (2001) Laser-induced time-resolved
738 luminescence as a tool for rare-earth element identification in minerals. Physics and
739 Chemistry of Minerals, 28, 347–363.
740
741 Gaft, M., Reisfeld, R., and Panczer, G. (2015) Modern Luminescence Spectroscopy of
742 Minerals and Materials, 2nd ed, 431 p. Springer International Publishing.
743
744 Gaft, M., Reisfeld, R., Panczer, G., Shoval, S., Champagnon, B., and Boulon, G. (1997) Eu^{3+}
745 luminescence in high-symmetry sites of natural apatite. Journal of Luminescence, 72–74,
746 572–574.
747
748 Gomez-Morales, J., Iafisco, M., Delgado-Lopez, J.M., Sarda, S., and Drouet, C. (2013)
749 Progress on the preparation of nanocrystalline apatites and surface characterization: Overview
750 of fundamental and applied aspects. Progress in Crystal Growth and Characterization of
751 Materials, 59, 1-46.
752
753 Harlov, D.E. (2015) Apatite: A Fingerprint for Metasomatic Processes. Elements, 11, 171–
754 176.
755
756 Hosseini, S.M., Drouet, C., Al-Kattan, A., and Navrotsky, A. (2014) Energetics of lanthanide-
757 doped calcium phosphate apatite. American Mineralogist, 99, 2320–2327.
758
759 Hughes, J.M., and Rakovan, J. (2002) The Crystal Structure of Apatite, $Ca_5(PO_4)_3(F,OH,Cl)$.
760 Reviews in Mineralogy and Geochemistry, 48, 1–12.
761
762 Hughes, J.M., and Rakovan, J.F. (2015) Structurally Robust, Chemically Diverse: Apatite and
763 Apatite Supergroup Minerals. Elements, 11, 165–170.
764
765 Jehlička, J., Culka, A., Bersani, D., and Vandenabeele, P. (2017) Comparison of seven
766 portable Raman spectrometers: beryl as a case study. Journal of Raman Spectroscopy, 48,
767 1289–1299.
768

Knutson, C., Peacor, D.R., and Kelly, W.C. (1985) Luminescence, color and fission track zoning in apatite crystals of the Panasqueira tin-tungsten deposit, Beira-Baixa, Portugal. American Mineralogist, 70, 829–837.

Kottaisamy, M., Jagannathan, R., Jeyagopal, P., Rao, R.P., and Narayanan, R. (1994) Eu^{2+} luminescence in $M_5(PO_4)_3X$ apatites, where M is Ca^{2+}, Sr^{2+} and Ba^{2+}, and X is F^-, Cl^-, Br^- and OH^-. Journal of Physics D: Applied Physics, 27, 2210–2215.

Lakowicz, J.R. (2006) Plasmonics in Biology and Plasmon-Controlled Fluorescence. Plasmonics, 1, 5–33.

Lenz, C., and Nasdala, L. (2015) A photoluminescence study of REE^{3+} emissions in radiation-damaged zircon. American Mineralogist, 100, 1123–1133.

Lenz, C., Nasdala, L., Talla, D., Hauzenberger, C., Seitz, R., and Kolitsch, U. (2015) Laser-induced REE^{3+} photoluminescence of selected accessory minerals — An "advantageous artefact" in Raman spectroscopy. Chemical Geology, 415, 1–16.

Marfunin, A.S. (1979) Spectroscopy, Luminescence and Radiation Centers in Minerals. 356 p. Springer Verlag Berlin, Heidelberg, New York.

Maurice, S., Wiens, R.C., Bernardi, P., and others (2021) The SuperCam Instrument suite on the Mars 2020 Rover: Science objectives and Mast-Unit Description. Space Science Reviews 217, 47.

McCubbin, F.M., and Jones, R.H. (2015) Extraterrestrial Apatite: Planetary Geochemistry to Astrobiology. Elements, 11, 183–188.

Meza, O., Villabona-Leal, E.G., Diaz-Torres, L.A., Desirena, H., Rodríguez-López, J.L., and Pérez, E. (2014) Luminescence Concentration Quenching Mechanism in Gd2O3:Eu^{3+}. The Journal of Physical Chemistry A, 118, 1390–1396.

Mondéjar, S.P., Kovtun, A., and Epple, M. (2007) Lanthanide-doped calcium phosphate nanoparticles with internal chystallinity and with a shell of DNA as fluorescent probes in cell experiments. Journal of Materials Chemistry, 17, 4153-4159.

Morozov, A.M., Morozova, L.G., Trofimov, A.K., and Feofilov, P.P. (1970) Spectral and luminescent characteristics of fluorapatite single crystals activated by rare-earth ions. Optika i Spektroskopiya, 29, 1106–1118.

Nasdala, L., Beyssac, O., William Schopf, J., Bleisteiner, B. (2012) Application of Raman-based images in the Earth sciences, in: Zoubir, A. (Ed.), Raman Imaging: Techniques and Applications, p. 145–187, Springer Series in Optical Sciences. Springer Berlin Heidelberg, Berlin, Heidelberg.

Nasdala, L., Smith, D.C., Kaindl, R., Ziemann, M.A. (2004) Raman spectroscopy: Analytical perspectives in mineralogical research, in: Papp, G., Weiszburg, T.G., Beran, A., Libowitzky, E. (Eds.), Spectroscopic Methods in Mineralogy p. 281–343. Mineralogical Society of Great Britain and Ireland, Germany.

O'Shea, D.C., Bartlett, M.L., and Young, R.A. (1974) Compositional analysis of apatites with Laser-Raman spectroscopy: (OH,F,Cl)apatites. Archives of Oral Biology, 19, 995–1006.

Panczer, G., De Ligny, D., Mendoza, C., Gaft, M., Seydoux-Guillaume, A.-M., Wang, X. (2012) Raman and fluorescence. In: Dubessy, J., Caumon, M-C., Rull, F. (eds) Raman Spectroscopy Applied to Earth Sciences and Cultural Heritage, p. 61-82, European Mineralogical Union and Mineralogical Society of Great Britain & Ireland, London.

Panczer, G., Gaft, M., Reisfeld, R., Shoval, S., Boulon, G., and Champagnon, B. (1998) Luminescence of uranium in natural apatites. Journal of Alloys and Compounds, 275–277, 269–272.

Pasteris, J.D., and Beyssac, O. (2020) Welcome to Raman Spectroscopy: Successes, Challenges, and Pitfalls. Elements, 16, 87-92.

Rakovan, J.F., and Pasteris, J.D. (2015) A Technological Gem: Materials, Medical, and Environmental Mineralogy of Apatite. Elements, 11, 195–200.

Reisfeld, R., Gaft, M., Boulon, G., Panczer, C., and Jørgensen, C.K. (1996) Laser-induced luminescence of rare-earth elements in natural fluor-apatites. Journal of Luminescence, 69, 343–353.

Rey, C., Marsan, O., Combes, C., Drouet, C., Grossin, D., and Sarda, S. (2014) Characterization of Calcium Phosphates Using Vibrational Spectroscopies. In: Ben-Nissan B. (ed) Advances in Calcium Phosphate Biomaterials p. 229-266. Springer Series in Biomaterials Science and Engineering, vol 2. Springer, Berlin, Heidelberg.

Suarez C.A., Machpherson G.L., González L.A., and Grandstaff D.E. (2010) Heterogeneous rare earth element (REE) patterns and concentrations in a fossil bone: Implications for the use of REE in vertebrate taphonomy and fossilization history. Geochimica and Cormochimica Acta 74, 2970-2988.

Sun, S.-S. and McDonough, W.-S. (1989) Chemical and isotopic systematics of oceanic basalts: implications for mantle composition and processes. Geological Society, London, Special Publications, 42, 313-345.

Syassen, K. (2008) Ruby under pressure. High Pressure Research, 28, 75-126.

Waychunas, G.A. (2014) Luminescence Spectroscopy. Reviews in Mineralogy and Geochemistry, 78, 175–217.

Waychunas, G.A. (2002) Apatite Luminescence. Reviews in Mineralogy and Geochemistry, 48, 701–742.

Webster, J.D., and Piccoli, P.M. (2015) Magmatic Apatite: A Powerful, Yet Deceptive, Mineral. Elements, 11, 177–182.

Wiens, R.C., Maurice, S., Robinson, S.H., and others (2021) The SuperCam Instrument Suite on the NASA Mars 2020 Rover: Body Unit and Combined System Tests. Space Science Reviews 217, 4.

Figures Caption

Figure 1: Chondrite-normalized REE patterns from ICP-MS analysis of natural apatites (normalization factor from Sun and McDonough,1989).

Figure 2: XRD diffractograms for the synthetic hydroxylapatites doped with Eu at increasing concentration (see Table 2 for measured concentration). Similar crystallinity was obtained for the other samples doped with Sm, Dy and Nd.

Figure 3: Fourier Transform Infrared spectra for synthetic hydroxylapatites doped with Eu at increasing concentrations (see Table 2 for measured concentrations). Similar crystallinity was obtained for the other samples doped with other with Sm, Dy and Nd.

Figure 4: Representative continuous-wave Raman and luminescence spectra of synthetic hydroxylapatites doped with Eu (a), Sm (b), Dy (c), and Nd (d). All spectra are raw data, excitation at 532 nm except for Nd (785 nm) and are acquired with the same acquisition time for each series. Note the strong background affecting the spectrum Sm2. R indicates a Raman peak.

Figure 5: Representative Raman spectra obtained on an hydroxylapatite doped with 23,936 ppm of Sm. The continuous-wave spectrum was obtained with the time-resolved instrument by opening the gate for 450,000 ns (nearly pulse to pulse at 2 KHz) and including the laser pulse. The luminescence signal from Sm significantly masks the Raman signal. The time-resolved spectrum was obtained with the time-resolved instrument by opening the gate for 5 ns including the laser pulse. The luminescence signal from Sm is completely rejected and the Raman signal is clearly visible.

Figure 6: Representative continuous-wave (green, ICCD gate of 450,000 ns including the laser pulse) and time-resolved (red, ICCD gate of 5 ns centered on the laser pulse) Raman spectra of some natural apatites. All spectra are raw data.

Figure 7: Time-resolved Raman and luminescence spectra obtained on the Durango apatite by using various combinations of delay and gates for the ICCD. From top to bottom green (Raman + all luminescence) is obtained with a long gate (450,000 ns) including the laser

pulse. Red (Raman only) is obtained with a short gate (5 ns) including the laser pulse. Black (all luminescence, no Raman) is obtained with a long gate (450,000 ns) opened just after the laser pulse (10 ns). Pale grey (short lifetime luminescence) is obtained with a gate of 1,500 ns opened just after the laser pulse (5 ns). Dark grey (long lifetime luminescence) is obtained with a long gate (450,000 ns) opened 1,500 ns after the laser pulse.

Figure 8: Time-resolved luminescence spectra obtained on the Durango apatite by using a constant delay (laser pulse not included so no Raman) and increasing progressively the opening of the ICCD gate.

Figure 9: Diagrams showing the area of the luminescence bands versus the doping element concentration for the 620 nm emission band for Eu (a) and the 600 nm emission band for Sm (b). The grey inset zooms on the same diagram at low concentration (<3,000 ppm).

Figure 10: Result of the time-sweep experiment for Eu- and Sm-doped hydroxylapatites (see Table 2 for the measured concentration). The plots depict the normalized intensity of the 620 nm emission band for Eu (a) and 600 nm emission band for Sm (b) versus the delay of the ICCD gate. This figure illustrates the time decay of the luminescence signal for Eu (a) and Sm (b). Lifetime is calculated as the slope of the line going through the experimental points.

Figure 11: Compilation of the lifetime of the luminescence for Eu (a) and Sm (b) versus the concentration in activator Eu and Sm, respectively, for the synthetic REE-doped (black circles) and natural apatites (colored squares).

This is the peer-reviewed, final accepted version for American Mineralogist, published by the Mineralogical Society of America.
The published version is subject to change. Cite as Authors (Year) Title. American Mineralogist, in press.
DOI: https://doi.org/10.2138/am-2022-8006. http://www.minsocam.org/

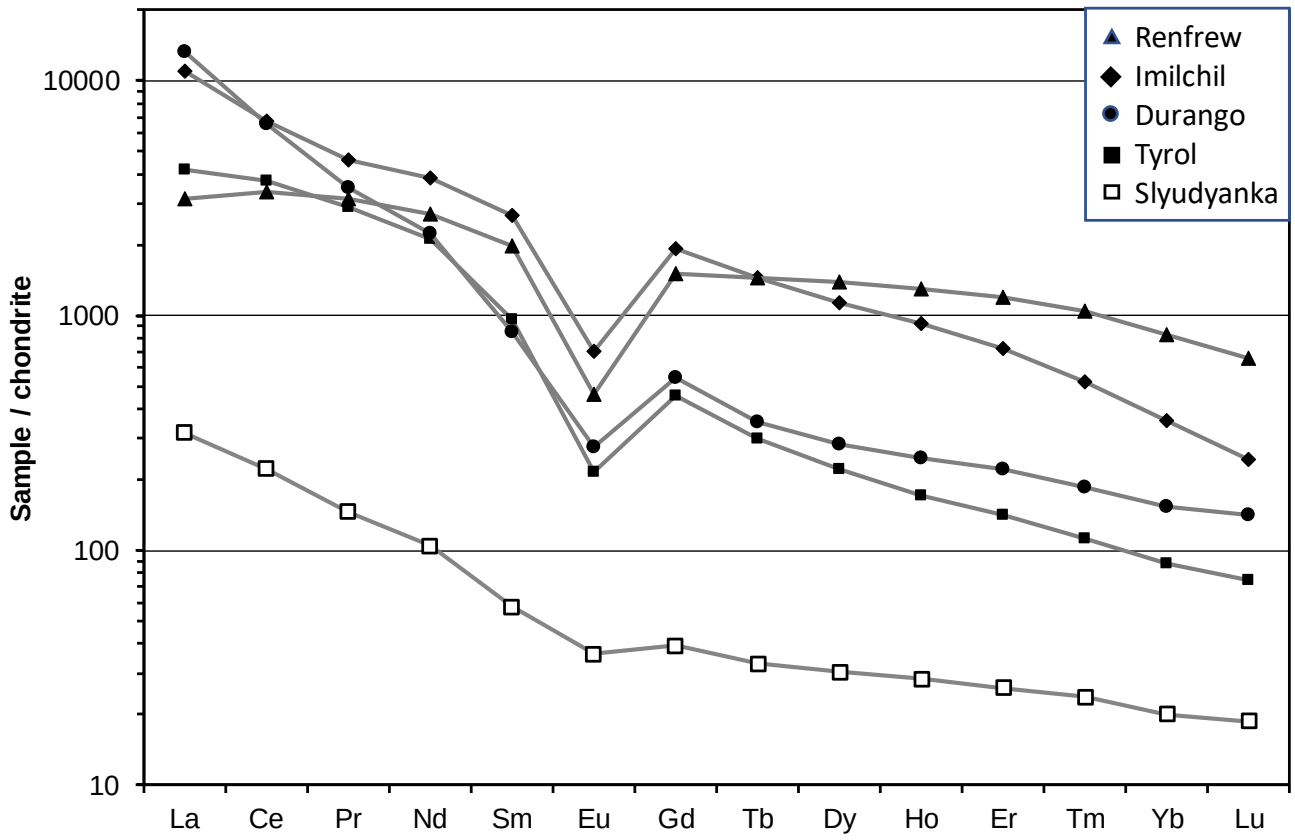

Figure 1

This is the peer-reviewed, final accepted version for American Mineralogist, published by the Mineralogical Society of America.
The published version is subject to change. Cite as Authors (Year) Title. American Mineralogist, in press.
DOI: https://doi.org/10.2138/am-2022-8006. http://www.minsocam.org/

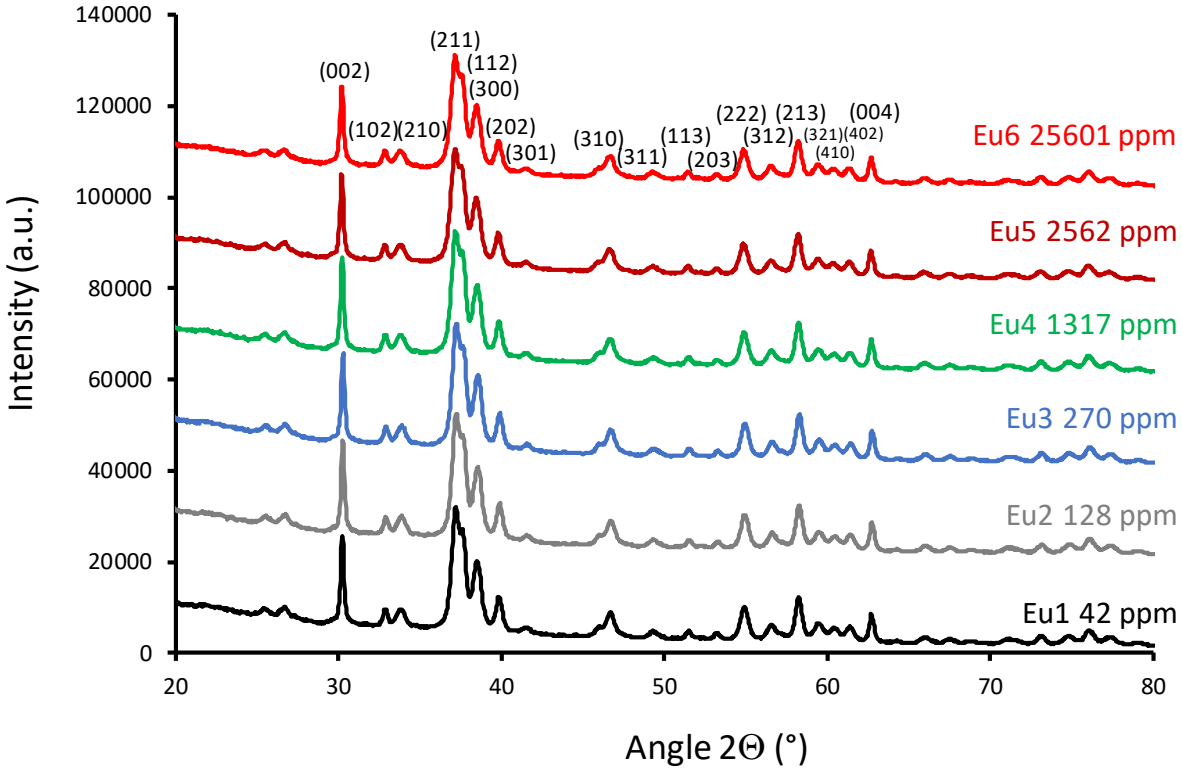

Figure 2

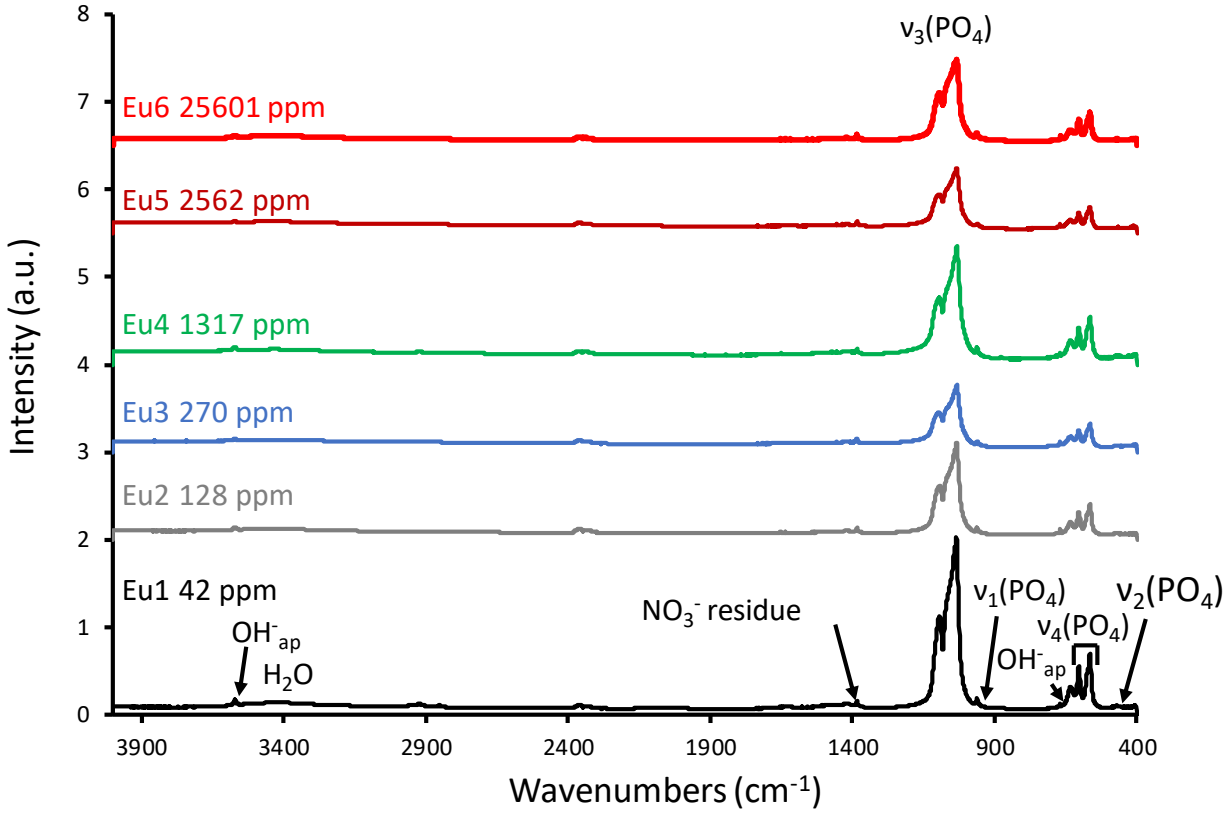

Figure 3

This is the peer-reviewed, final accepted version for American Mineralogist, published by the Mineralogical Society of America.
The published version is subject to change. Cite as Authors (Year) Title. American Mineralogist, in press.
DOI: https://doi.org/10.2138/am-2022-8006. http://www.minsocam.org/

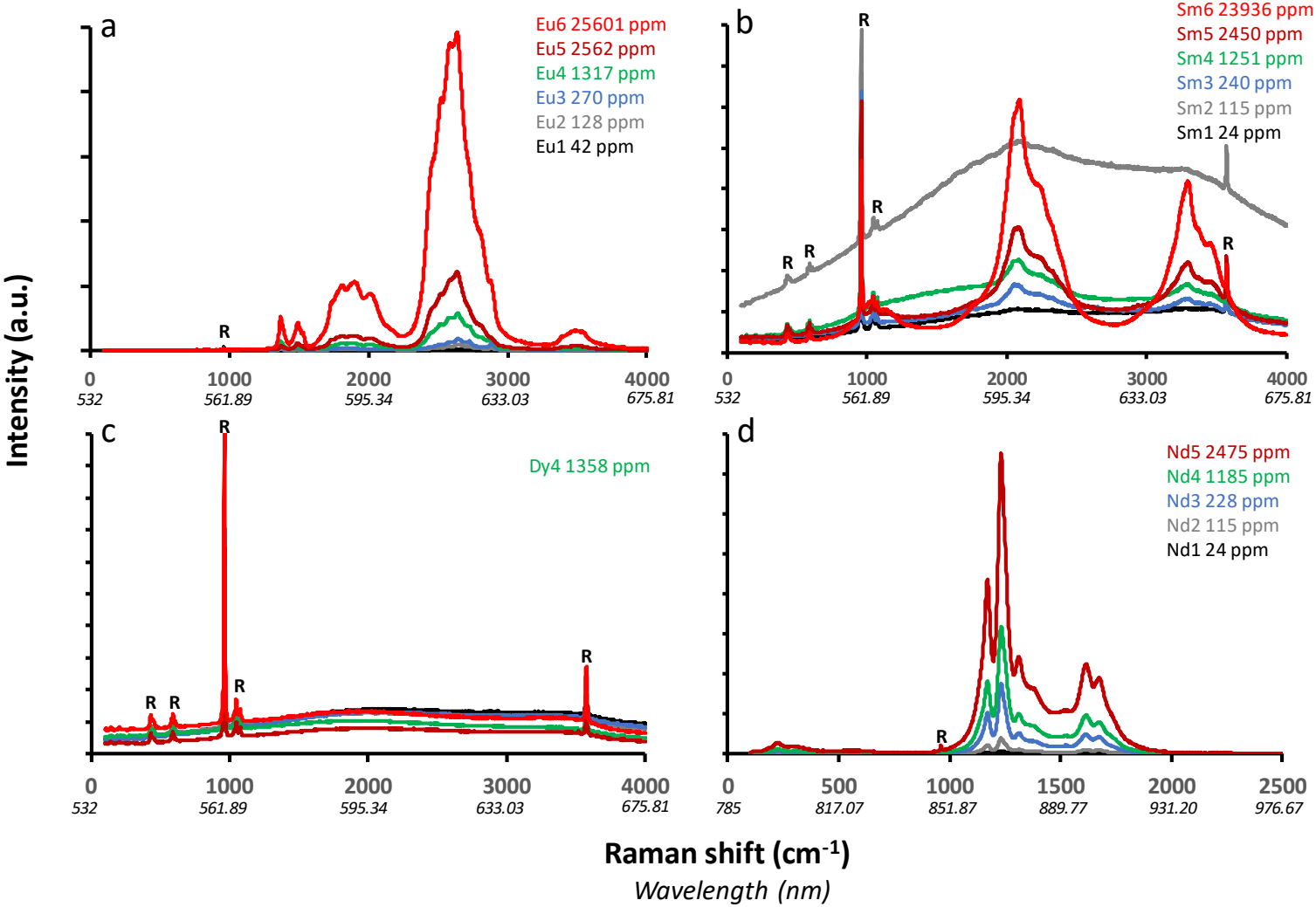

Figure 4

This is the peer-reviewed, final accepted version for American Mineralogist, published by the Mineralogical Society of America.
The published version is subject to change. Cite as Authors (Year) Title. American Mineralogist, in press.
DOI: https://doi.org/10.2138/am-2022-8006. http://www.minsocam.org/

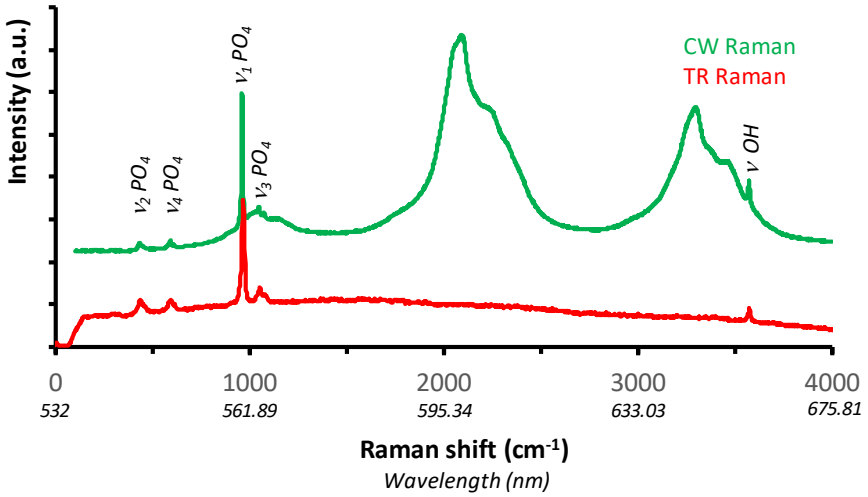

Figure 5

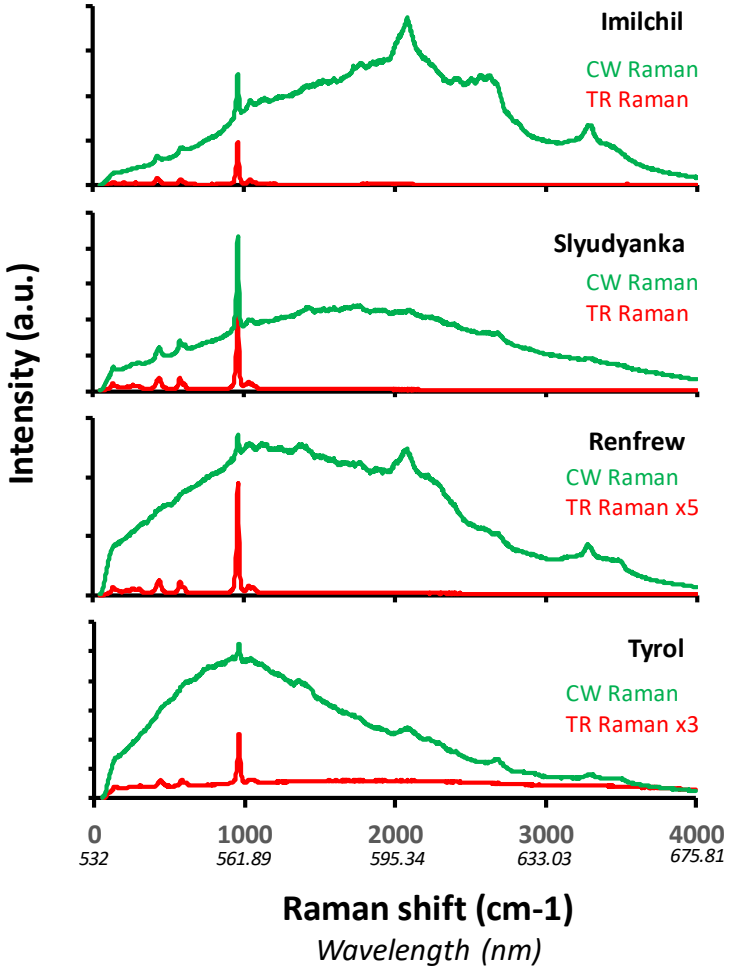

Figure 6

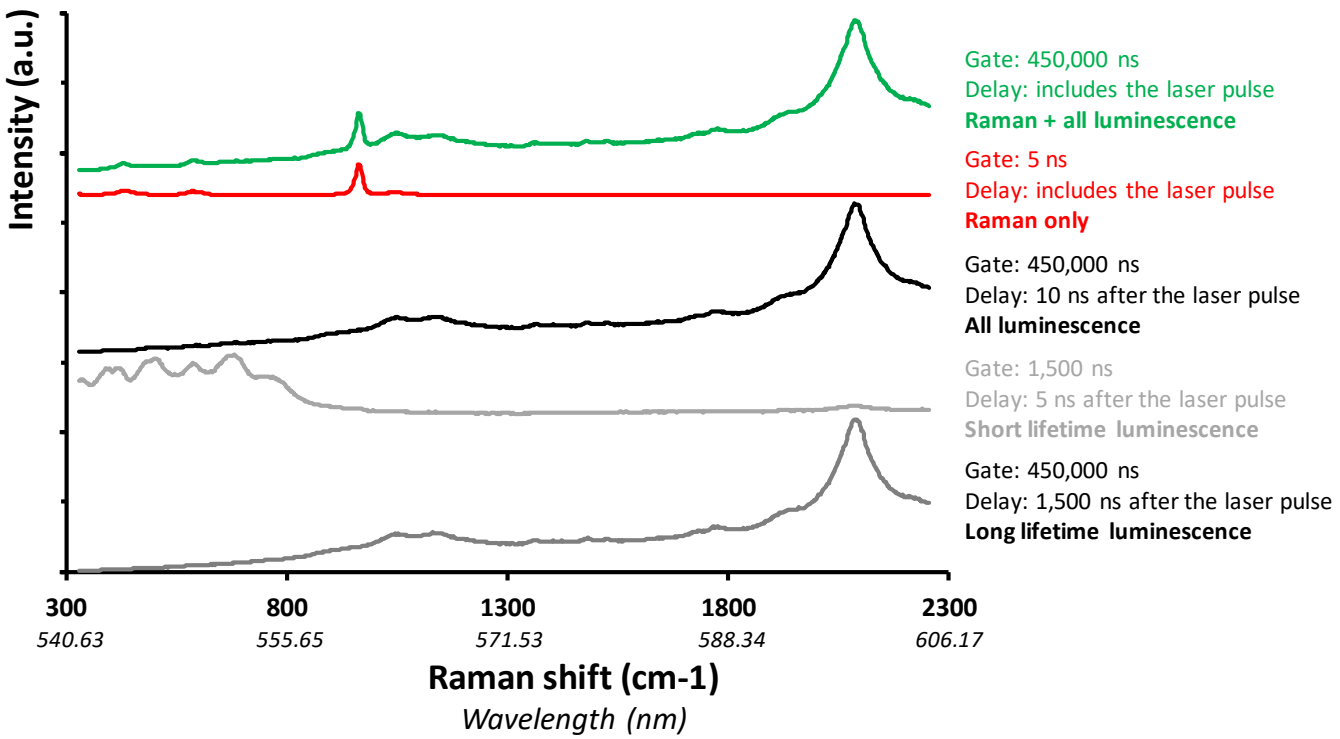

Figure 7

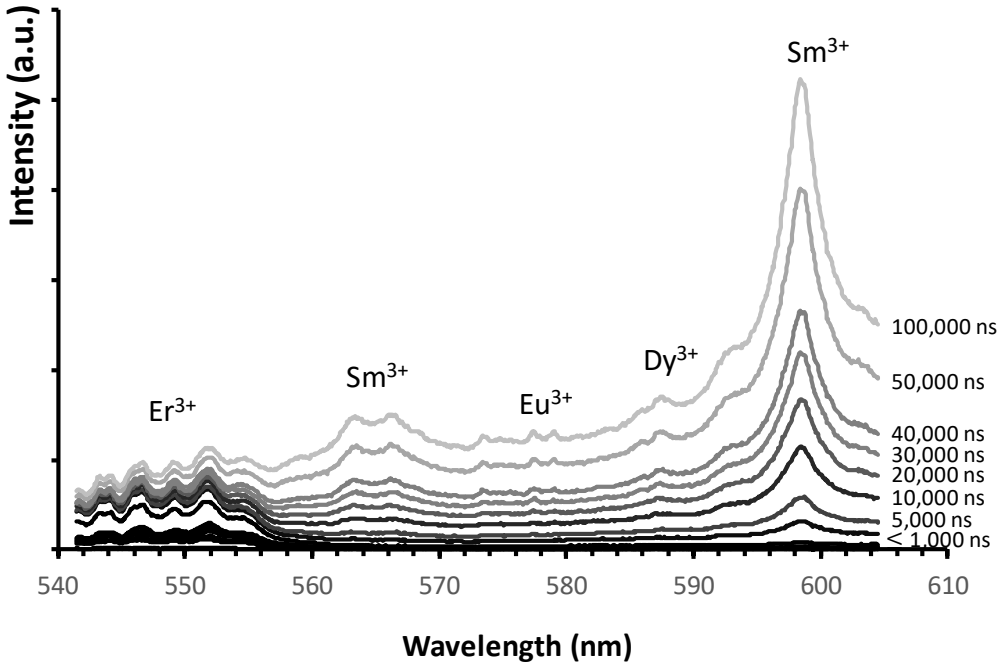

Figure 8

This is the peer-reviewed, final accepted version for American Mineralogist, published by the Mineralogical Society of America.
The published version is subject to change. Cite as Authors (Year) Title. American Mineralogist, in press.
DOI: https://doi.org/10.2138/am-2022-8006. http://www.minsocam.org/

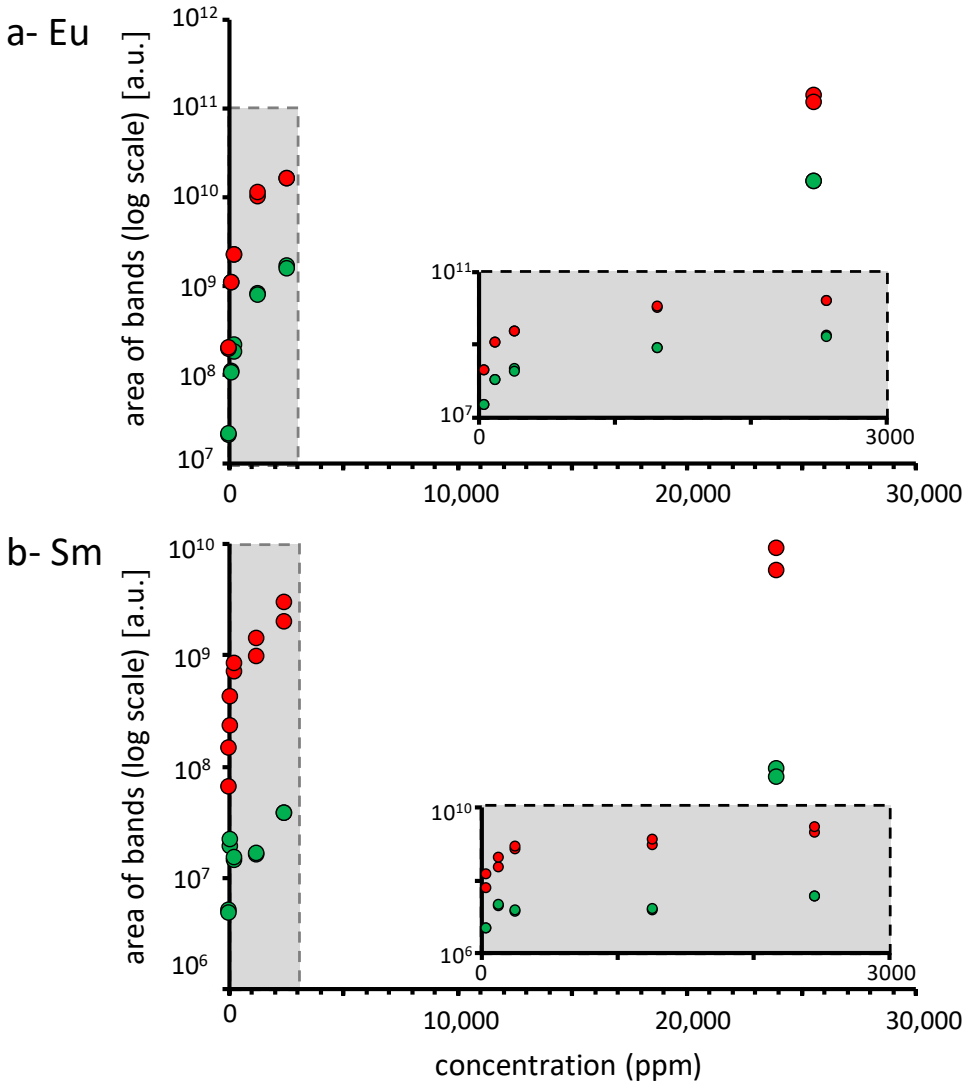

Figure 9

This is the peer-reviewed, final accepted version for American Mineralogist, published by the Mineralogical Society of America.
The published version is subject to change. Cite as Authors (Year) Title. American Mineralogist, in press.
DOI: https://doi.org/10.2138/am-2022-8006. http://www.minsocam.org/

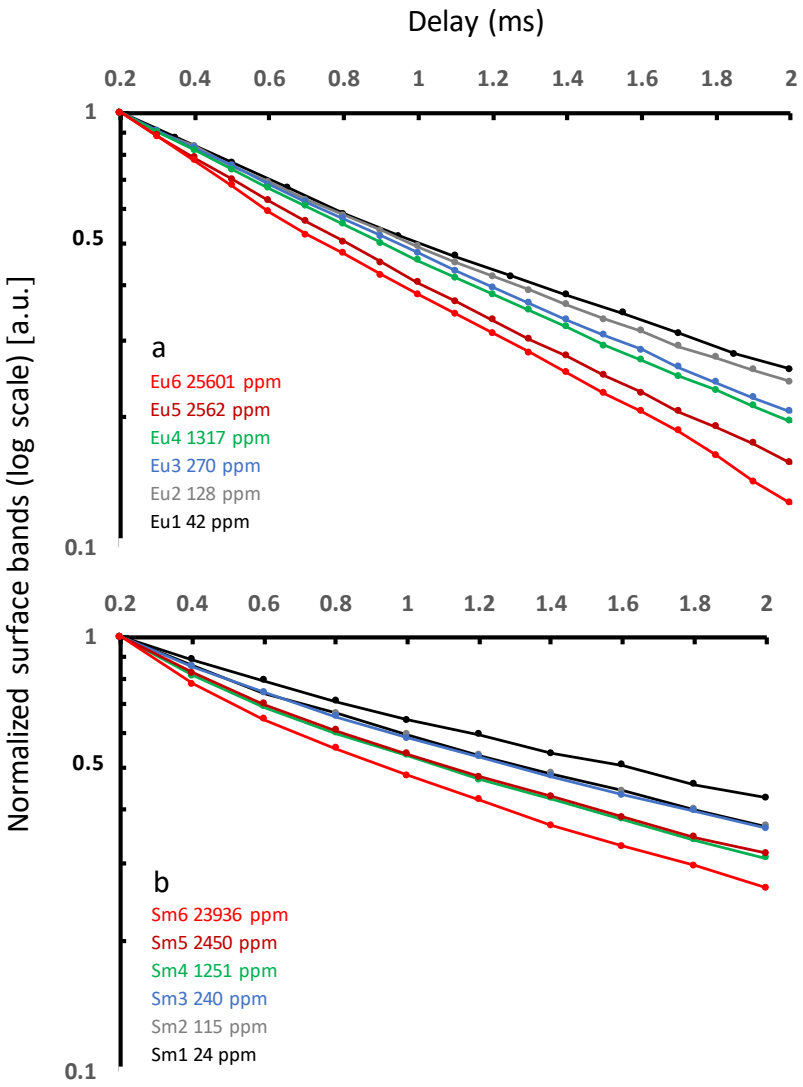

Figure 10

This is the peer-reviewed, final accepted version for American Mineralogist, published by the Mineralogical Society of America.
The published version is subject to change. Cite as Authors (Year) Title. American Mineralogist, in press.
DOI: https://doi.org/10.2138/am-2022-8006. http://www.minsocam.org/

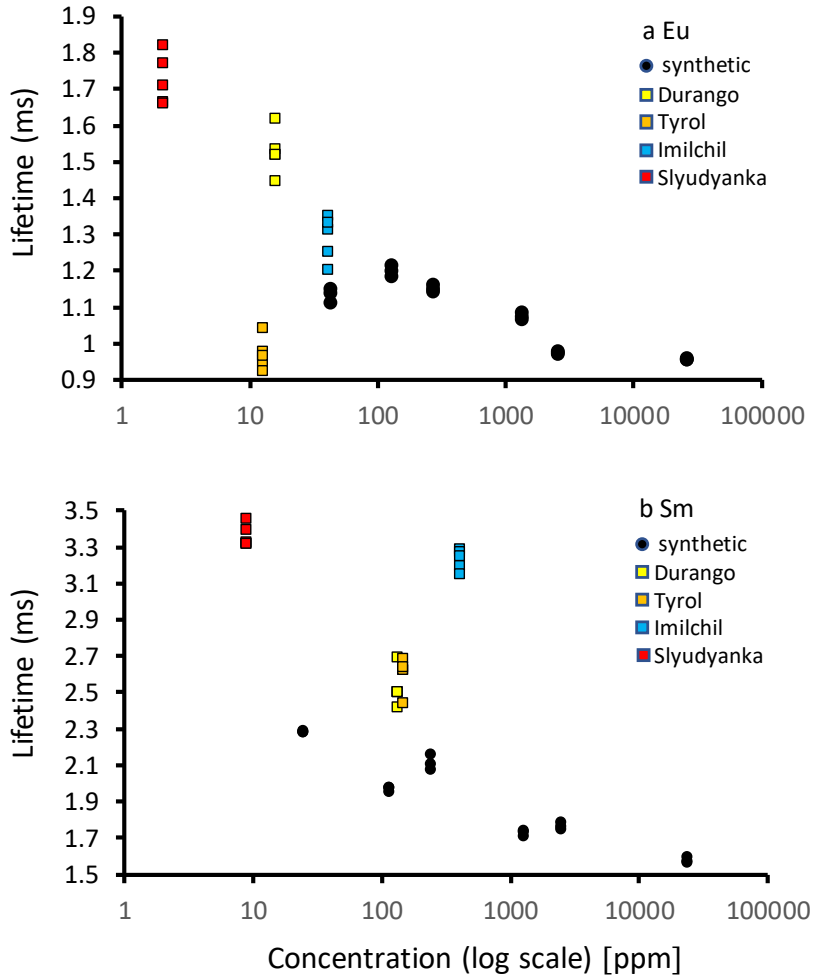

Figure 11

This is the peer-reviewed, final accepted version for American Mineralogist, published by the Mineralogical Society of America.
The published version is subject to change. Cite as Authors (Year) Title. American Mineralogist, in press.
DOI: https://doi.org/10.2138/am-2022-8006. http://www.minsocam.org/

Table 1: Nd, Sm, Eu and Dy composition of the synthetic hydroxyapatite samples measured by ICP-MS. (µg/g = ppm; < L.D below limit of detection).

Sample reference	Nd µg/g	Sm µg/g	Eu µg/g	Dy µg/g	CaO wt%	P_2O_5 wt%
Eu 1	0	0	42	0	53.02	39.01
Eu 2	0	0	128	0	53.06	38.92
Eu 3	0	< L.D.	270	0	53.34	39.36
Eu 4	0	0	1 317	0	52.80	38.63
Eu 5	0	0	2 562	0	52.33	37.87
Eu 6	0	0	25 601	0	50.02	37.36
Sm 1	0	24	5	0	52.77	39.17
Sm 2	0	115	5	0	52.06	37.89
Sm 3	0	240	1	0	53.31	39.82
Sm 4	0	1 251	0	0	52.35	38.47
Sm 5	0	2 450	0	0	52.37	38.31
Sm 6	0	23 936	1	1	50.06	37.13
Nd 1	24	4	< L.D.	0	52.91	38.83
Nd 2	115	1	< L.D.	0	52.46	38.14
Nd 3	228	0	< L.D.	1	52.81	38.84
Nd 4	1 185	3	2	2	53.16	39.03
Nd 5	2 475	0	0	5	52.57	38.45
Nd 6	24 832	2	1	50	50.59	39.91
Dy 4	4	< L.D.	0	1 358	51.89	38.16

This is the peer-reviewed, final accepted version for American Mineralogist, published by the Mineralogical Society of America.
The published version is subject to change. Cite as Authors (Year) Title. American Mineralogist, in press.
DOI: https://doi.org/10.2138/am-2022-8006. http://www.minsocam.org/

Table 2: Major elements (oxide wt%) and REE composition (μg/g or ppm) of the natural apatite samples measured by ICP-MS (< L.D below limit of detection).

	Tyrol	**Imilchil**	**Renfrew**	**Slyudyanka**	**Durango**
Location	Tyrol – Austria	Imilchil – Morocco	Renfrew, Ontario – USA	Lake Baikal, Russia	Durango – Mexico
Type	fluorapatite	fluorapatite	fluorapatite	unknown	fluorapatite
Form	polycristal	polycristal	polycristal	polycristal	monocristal
Color	dark green	light green – yellow	light green	light blue	yellow
CaO	53.23	53.35	54.11	54.34	53.58
P_2O_5	39.83	41.47	40.72	39.92	40.68
MnO	< L.D.	0.02	0.11	< L.D.	< L.D.
Sc	2	1	1	< L.D.	1
Y	297	1418	1643	46	452
La	992	2590	741	75	3166
Ce	2290	4138	2058	136	4030
Pr	276	438	297	14	332
Nd	994	1794	1264	49	1045
Sm	147	407	302	9	131
Eu	13	41	27	2	16
Gd	94	397	308	8	112
Tb	11	54	55	1	13
Dy	56	286	353	8	72
Ho	10	52	74	2	14
Er	23	119	197	4	37
Tm	3	13	27	1	5
Yb	15	61	141	3	26
Lu	2	6	17	0	4